*Battery Energy*

WILEY

BATTERY ENERGY Open Access

RESEARCH ARTICLE OPEN ACCESS

# Advancing the Technology of Lithium, Magnesium, and Aluminum-Ion Batteries via Chromium Ditelluride as a Novel Anode Material

Abdul Majid[1] | Hafsa Raza[1] | Sawaira Tasawar[1] | Hira Batool[1] | Mohammad Alkhedher[2] | Salahuddin Khan[3] | Kamran Alam[4]

[1]Department of Physics, University of Gujrat, Gujrat, Pakistan | [2]Department of Mechanical and Industrial Engineering, Abu Dhabi University, Abu Dhabi, United Arab Emirates | [3]College of Engineering, King Saud University, Riyadh, Saudi Arabia | [4]Department of Chemical Engineering Materials Environment Sapienza, University of Rome, Italy

**Correspondence:** Abdul Majid (abdulmajid40@uog.edu.pk) | Kamran Alam (Kamran.alam@uniroma1.it)

**Received:** 5 August 2024 | **Revised:** 11 October 2024 | **Accepted:** 1 December 2024

**Funding:** This study was supported by Abu Dhabi University's Office of Research and Sponsored Programs (Grants 19300638 and 19300791) and the authors sincerely appreciate funding from Researchers Supporting Project number (RSP2025R58), King Saud University, Riyadh, Saudi Arabia.

**Keywords:** aluminum-ion battery | anode | $CrTe_2$ | density functional theory | diffusion barrier | lithium-ion battery | magnesium-ion battery | metal-ion battery | open-circuit voltage | storage capacity

## ABSTRACT

The pursuit of novel anode materials that offer high storage capacity, hasty ionic transport, good cyclic stability, and material recyclability is at the core of the research activities. In this study, we uncovered the potential of 2D puckered chromium ditelluride ($CrTe_2$) as a novel anode material for multivalent metal-ion batteries employing Li ions, Mg ions, and Al ions. The structural and dynamical stability of the material was ensured via formation energy and phonon dispersion curves. The optimal anodic properties of the material were systematically analyzed, with a focus on its structural properties, electronic characteristics, adsorption sites, diffusion barriers, and storage capability. The exothermic interactions of Li, Mg, and Al with host $CrTe_2$ demonstrated its suitability for the intercalation process in respective monovalent, divalent, and trivalent ion batteries. The storage capacity of the material appeared as 1745 mAh $g^{-1}$ for LIBs, 872 mAh $g^{-1}$ for MIBs, and 785 mAh $g^{-1}$ for AIBs. The open-circuit voltage is found as 0.76 V for Li, 0.97 V for Mg, and 0.62 V for Al. The diffusion barriers faced by Li, Mg, and Al atoms are found to be low at 0.26 eV, 0.55 eV, and 0.42 eV, respectively, which points to the rapid charging capability of the battery. Furthermore, the electronic transport properties of the host material are also studied using a combined density functional theory (DFT) and Green's function method (DFT-GF). The findings of this study indicate that $CrTe_2$ has the potential for utilization as a promising anode material for the development of high-performance Li, Mg, and Al-ion batteries.

## 1 | Introduction

The extensive use of fossil fuel-based sources, including petroleum, coal, and gas, is not only causing economic and environmental problems but also cautions to disturb the global demand/supply balance in the near future. These considerations require a technological transition from conventional sources to sustainable, renewable, environmentally friendly energy solutions [1]. However, current technologies lack large-scale implementation of the available solutions in the majority of electronic applications, electrical vehicles, and electrical grids. The rechargeable metal-ion batteries offer several advantages over contemporary sources owing to their improved electrochemical performance,

reduced environmental impact, portability, cost-effectiveness, and greater application versatility [2, 3].

The batteries, including lithium-ion batteries (LIBs), magnesium-ion batteries (MIBs), and aluminum-ion batteries (AIBs), are trending energy storage devices these days. There have been significant reported efforts and success in realizing and commercializing LIBs, but these still face issues such as low energy density, low functional life, safety, and material abundance, which need to be addressed. NIBs and KIBs are still in the early stages of development and their electrochemical characteristics are inferior due to lower energy densities and shorter cycle lifespans compared to LIBs. Hence, the current market and research activities exhibit the dominance of LIBs as the preferred option for the majority of energy storage applications [4, 5]. An increasing trend in the utilization of LIBs in portable electronic devices, stationary energy storage elements, and electric vehicles is being observed [4, 6]. The features of LIBs that recognize them as leading energy storage devices include their long cycle life, low self-discharge, low cost, fast charging, lightweight, low maintenance, high energy, and power density [7–9]. The primary mechanism of LIBs involves transferring lithium ions between the cathode and anode during the charging and discharging process [10].

The selection of anode material in LIBs is crucial in determining storage capacity, voltage profile, and stability [11, 12]. Graphite is a commercially used anode material in LIBs, which offers a theoretical capacity of 372 mAh $g^{-1}$ with a lifespan of 500 cycles [13, 14]. Silicon is a potential anode with a very high theoretical capacity of 4200 mAh $g^{-1}$ in LIBs but a shorter cycle life of 100 cycles due to a significant volume expansion of about 300% that leads to structural deformation and capacity losses [15–17]. Tin has also been used as anode material with a theoretical capacity of 994 mAh $g^{-1}$ with a life span of about 500 cycles [18, 19]. Graphene has been found to offer a theoretical capacity higher than graphite (i.e., 400–1300 mAh $g^{-1}$) due to which it exhibits superior potential for storage in LIB [6, 17].

While moving beyond LIBs, the multivalent ion batteries such as MIBs and AIBs that utilize $Mg^{2+}$ and $Al^{3+}$ ions offer the capability to achieve the storage capacity using just one-half and one-third metal ions, respectively. Hence, the utilization of higher valent ions may produce lightweight batteries with higher storage capacity and higher material abundance. The Al atom offering $Al^{3+}$ ions is an attractive choice for metal-ion batteries due to its abundance, physical, and chemical properties. Its properties make it stable and less reactive at elevated temperatures, reducing the risk of thermal runaway and other safety issues. Its high electronegativity enhances stability and resistance to degradation, improving the performance and lifespan of AIBs. The AIBs emerge as a promising alternative for grid-level stationary energy storage due to their cost-effectiveness, ample raw material availability, extended cycle longevity, and environmentally friendly character. A notable electrolyte option for AIBs is chloroaluminate ionic liquid (IL), consisting of $AlCl_3$ and a Lewis basic organic chloride. This electrolyte system is commonly used in AIBs and often functions as an electroactive anode material. Ng et al. investigated the impact of $AlCl_3$−XCl Ionic Liquids on AIBs [20]. In contrast, MIBs offer a safe, efficient, and dependable storage device than LIBs due to higher electrochemical properties, less likelihood of dendritic formation, and higher stability of anodes even in humid settings [21]. The metals offering multivalent ions are far more abundant in the earth's crust than lithium, which ensures the production of low-price batteries for large-scale utilization. Hence, the technological advancement in realizing MIBs and AIBs is expected to settle the current issues related to energy density, cost-effectiveness, and battery safety [22, 23].

The 2D materials are known to be viable anode materials for use in metal-ion batteries due to their unique high electrical conductivity, large surface area, good mechanical properties, and low volume expansion [4, 11]. The exploration of novel 2D materials including transition metal chalcogenides, transition metal dichalcogenides (TMDs), transition metal oxides (TMOs), and transition metal carbonates (TMCs) for use as anode material in the batteries is in progress [24, 25]. These materials exhibit properties superior to graphene when storage capacity and metal-ion diffusion kinetics are taken into account. The preliminary encouraging outcomes have invited further investigation to explore more 2D anode materials to enhance the performance and commercial feasibility of batteries [26–28].

The selection of 2D puckered $CrTe_2$ as the anode material was motivated by its unique properties, including its layered structure, high surface area, and excellent electronic conductivity, which are advantageous for ion intercalation and charge transport. Additionally, previous studies on 2D TMDs have demonstrated their potential in energy storage applications, suggesting that $CrTe_2$ could offer promising performance as an anode material like 2D $MoTe_2$, which has emerged as a resourceful material for energy storage applications [29, 30]. $Cr_2Si_2Te_6$ and $Cr_2Ge_2Te_6$ are 2D materials beyond graphene that have been found suitable for storage applications with suitable properties [31]. Mn-oxides, V-oxides, and TMCs are examples of materials used in electrodes. Recently, novel families of electrodes featuring transformation mechanisms, such as chalcogen and halogen, have gained attention due to their predictable range of valence variations. Tellurium (and its tellurides) stand out as potential materials in this regard due to their superior structural and transport properties [32, 33].

The TMDs have been considered promising materials for various applications, but their utilization in LIBs has recently drawn attention [27, 34]. The classical TMDs appearing in the form of $MX_2$ typically consist of transition metals and non-metals, whereas the M sites are occupied by transition or d-block elements, and X contains chalcogen elements (S, Se, and Te). These TMDs are distinguished by their unique and organized 2D lattice structure (X–M–X) in which the transition metal and chalcogenide are periodically grouped in a hexagonal or trigonal configuration [13, 35]. The hexagonal structure of TMDs as 2D materials is not as thin as a single carbon atom sheet of graphene [36, 37]. $MoS_2$ is a renowned material because of its 2D structure that offers a theoretical capacity of 669 mAh $g^{-1}$ as an anode material for LIBs [13, 38]. Likewise, $WS_2$ and $MoTe_2$ exhibited storage capacity of 590 and 305 mAh $g^{-1}$, respectively [39, 40]. The reported values of storage capacity, open-circuit voltage (OCV), and diffusion barrier for famous 2D anode materials are listed in Table 2.

This study was planned with the motivation to explore novel anode materials in search of suitable structural and electronic character, high storage capacity, and enhanced ionic transport. Chromium-based dichalcogenides have received research attention due to their high natural abundance and requisite chemical and physical properties that make them attractive candidates for batteries [41]. $CrTe_2$ has a graphite-like van der Waals (vdW) layered structure, which indicates its potential for the intercalation of foreign atoms [42]. This study was carried out using density functional theory (DFT)-based methods to comprehensively investigate the potential of $CrTe_2$ as an anode material for multivalent ion batteries. Using the supercell approach, we calculated the fundamental, electronic, electrochemical, and transport properties of $CrTe_2$ with Li, Mg, and Al intercalation. The findings of this work indicate the potential of $CrTe_2$ as an intercalation material for use as an electrode in LIBs, MIBs, and AIBs. Notably, the low diffusion barriers for Li, Mg, and Al ions in the host are obtained, which suggest fast charging capabilities due to efficient ion movement. The exothermic interactions of the ions with the host highlight its suitability for the intercalation/de-intercalation process to assist charge/discharge cycles of the battery. The methodology and a detailed explanation of the findings are described in the following sections.

## 2 | Methodology

The work being reported comprises DFT-based calculations performed on pure and Li, Mg, and Al-intercalated $CrTe_2$ slabs performed using the BAND and DFTB modules of Amsterdam density functional (ADF) [43, 44]. The level of theory employed Pardew–Burke–Ernzerh (PBE) under generalized gradient approximation (GGA) functional [45, 46]. The vdW's interactions in the layered structure of the host were modeled using the dispersion-corrected Grimme D3 technique [47, 48]. The process of structural optimization was achieved through the Quasi-Newton approach to obtain energy minimum configuration. The interactions between periodic images of the slabs were avoided by sufficient vacuum thickness under periodic boundary conditions. Triple zeta polarized (TZP) basic functions were employed to expand the orbitals to ensure high numerical accuracy during the calculations [49, 50].

The phonon spectra of the host $CrTe_2$ were calculated to elucidate its dynamical stability. The dispersion curves dictate the lattice vibrations in the material, such that positive phonon modes refer to the dynamical stability of the host material.

The formation energy of the material was calculated by Equation (1).

$$E_{\text{formation}} = \frac{(\boldsymbol{E}_{\mathbf{CrTe_2}}) - (\boldsymbol{x}\boldsymbol{E}_{\mathbf{Cr}} + \boldsymbol{y}\boldsymbol{E}_{\mathbf{Te_2}})}{\boldsymbol{x} + \boldsymbol{y}} \quad (1)$$

where $E_{\text{CrTe2}}$ represents the optimized energy of the $CrTe_2$, whereas $E_{\text{Cr}}$ and $E_{\text{Te}_2}$ represent the energies of Cr and Te atoms, respectively. The variables $x$ and $y$ correspond to the number of atoms in the unit cell.

The process of intercalation is the foremost task in determining the suitability of a host as an anode of metal-ion batteries. The intercalation energy determines the nature of the electrochemical reaction, which was estimated by placing metal atoms at various high-symmetry locations. The negative values of adsorption energies were monitored to ensure exothermic events occurred during metal atom intercalation. The energetically suitable intercalation site was discovered by placing the metal atoms at all possible high symmetry sites in the host material. The lowest energy site is able to preferentially accommodate the metal atoms and study concentration-dependent behavior. The value of the energy to intercalate metal atoms into the host material $CrTe_2$ is determined using Equation (2) [51].

$$E_{\text{Intercalation}} = E_{X_n\text{CrTe}_2} - n \times E_X - E_{\text{CrTe}_2} \quad (2)$$

The intercalation energy of the metal atom added to the host structure is represented by the value $E_X$, the intercalated energy of $X$ atoms ($X$ = Li, Mg, and Al) in $CrTe_2$ is represented by $E_{X\text{CrTe}_2}$, and the optimum energy of the pure $CrTe_2$ structure is shown by $E_{\text{CrTe}_2}$. When the intercalation energies are negative, the reaction will be exothermic and used to determine the anode's storage capacity. The capacity of storing Li, Mg, and Al in the anode is the most important factor as it has a significant impact on the battery's overall efficiency. Equation (2) is used to determine the intercalation energy, which is then used to systematically introduce metal atoms into the host structure to determine the storage capacity. The primary task is to determine the storage capacity to test the feasibility of an anode for any rechargeable battery, as determined using Equation (3) [11, 14].

$$C = \frac{n\,z\,F}{M_{\text{CrTe}_2}} \quad (3)$$

In this equation, the mass of $CrTe_2$ is denoted by $M_{\text{CrTe}_2}$, and $n$ represents the number of metal atoms included in the simulation, where $z$ is the valence number ($z = 1$ for Li, $z = 2$ for Mg, and $z = 3$ for Al). The value of Faraday's constant is 26.801 Ah/mol.

The electrochemical efficiency of rechargeable batteries is determined via OCV whose calculations were carried out for $CrTe_2$ using Equation (4) [52]. Throughout the intercalation/deintercalation of metal ions in the host, the OCV determines the operating voltage of $CrTe_2$ as an anode [53]:

$$V = -\frac{E_{\text{intercalation}}}{z\text{e}} \quad (4)$$

where $E_{\text{int}}$ is the energy calculated according to Equation (2) for the metal atom-adsorbed $CrTe_2$, and $z$e represents the electronic charge of the ions in the electrolyte ($z = 1$ for Li ions, $z = 2$ for Mg ions, and $z = 3$ for Al ions).

To analyze Li/Mg/Al diffusion pathways in $CrTe_2$, we used climb image nudged elastic band (CI-NEB) simulations on symmetrical routes in the structure [54]. This method estimates energy barriers and identifies saddle points, providing insights into energy requirements and optimal diffusion channels [55, 56]. We precisely located saddle points by employing intermediate images technique and global optimization to enhance the understanding of the diffusion process in the host [57]. The force on each considered image is computed using Equation (5).

$$F_i = \left|F_i^s\right|_{\parallel} - |\nabla E(R_i)|_{\perp} \quad (5)$$

where $F_i$, $\left|F_i^s\right|_{\parallel}$ and $|\nabla E(R_i)|_{\perp}$ represent the sum of all the forces, spring restoring force, and actual force on the considered image "$i$," respectively. The maximum value of the force on the considered image is calculated by Equation (6).

$$F_{i\,\max} = \nabla E(R_{i\,\max}) + 2\nabla E\,|R_{i\,\max}|_{\parallel} \quad (6)$$

To investigate the current ($I$) and voltage ($V$) characteristics of the material, we performed NEGF calculations. The nonequilibrium Green's function (NEGF) formalism is a powerful theoretical framework used to study quantum transport in nanoscale devices [58]. It allows for the calculation of electronic properties under nonequilibrium conditions, providing insight into the behavior of electrons in response to external biases. Driven by the rapid progress in experimental work on realizing single-molecule nanodevices, approaches to molecular transport based on DFT in conjunction with the NEGF formalism have garnered significant attention in the literature in recent years [59, 60]. The method's appeal stems from DFT's ability to self-consistently treat realistic atomistic and molecular transport configurations from an ab initio quantum chemical description. This is paired with an intuitive mapping using Green's function formalism to a Landauer-type expression for the conductance and current [61]. One of the main advantages of this type of system modeling is that it allows us to locate the interface between the active part of the single-molecule system and the leads between metal layers. This interface is much better understood than the intricate geometries that may result in the binding of molecules to metals. It is thus possible to alter the specifics of these binding geometries without having to recalculate the contributions from the bulk contacts. A more nuanced point is that this method, according to Evers et al. [62], enables us to test convergence to transport properties that correspond to truly bulk-reservoir electrodes by enlarging the extended molecule. They have demonstrated this for tight-binding chains and cluster Au electrodes of different sizes. Moreover, we may consider basic polarization effects in the leads due to the metallic portions of the extended molecule. The current $I$ is then obtained using the Landauer–Büttiker formula:

$$I(V) = 2e/h \int T(E,V)(f(E-\mu_L) - f(E-\mu_R))dE \quad (7)$$

where $f(E)$ is the Fermi–Dirac distribution function for a given temperature, and $\mu_L$ ($\mu_R$) is $(\epsilon F - eV/2)$, and $\epsilon_F$ is the Fermi energy of the electrodes.

## 3 | Results and Discussion

The findings of this work to shed light on the structural, electronic, and electrochemical properties of $CrTe_2$ for use as an anode in LIBs, MIBs, and AIBs are described in the following sections.

### 3.1 | Structural Properties

The 4 × 4 supercell of the $CrTe_2$ slab composed of 96 atoms (32 Cr atoms and 64 Te atoms) was optimized to check the electrochemical performance of the material as an anode. The structure comprises a transition metal "B" sandwiched between two chalcogen atoms A, forming an A–B–A configuration. The transition metal Cr is merged between two chalcogen Te atoms in such a way that Cr and Te atoms are covalently connected in each layer [40]. The optimized crystal structure of the layered $CrTe_2$ is shown in Figure 1. From the top view, it is clear that the host possesses a standard hexagonal geometrical structure with the space group Pm1 with lattice parameters $a = b = 3.86$ Å, $c = 6.20$ Å, $\alpha = \beta = 90°$, and $\gamma = 120°$ [63]. The geometrical convergence of the host resulted in forming a layered structure with interlayer distances of 3.01 Å. The Cr–Te bond length was found to be 2.74 Å, which agrees with the reported theoretical findings [30]. $CrTe_2$ is a graphite-like structure with weak vdW forces between its layers [64]. From the side view, it is clear that one Cr layer is sandwiched within two Te because of the chemical proportion M:X being 1:2,

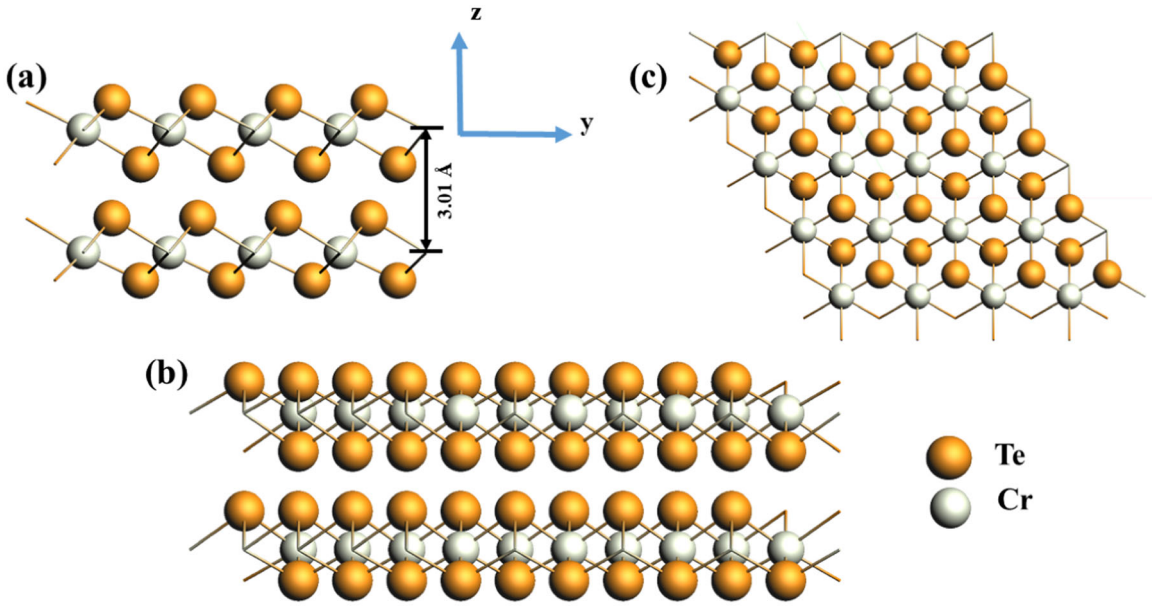


**FIGURE 1** | The structure of the host $CrTe_2$ viewed along (a) $x$-axis, (b) $y$-axis, and (c) $z$-axis.

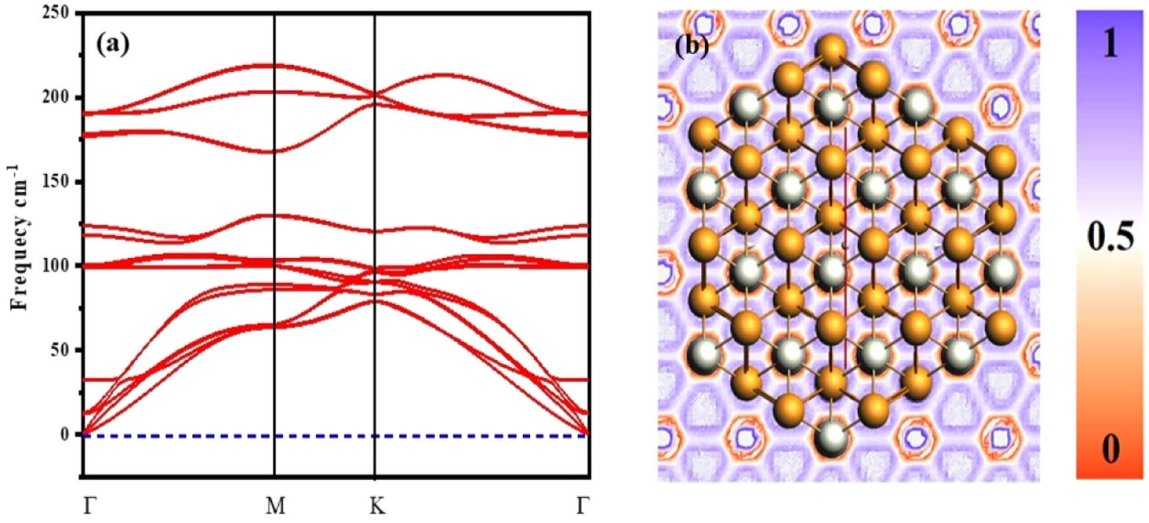


**FIGURE 2** | (a) The calculated phonon dispersion curves of $CrTe_2$. (b) The calculated electron localization function (ELF) map of pure $CrTe_2$ (sidebar indicates scale from 0 to 1 for charge value). The Cr and Te atoms are represented by gray and golden spheres.

illustrated in Figure 2b resulting in an X–M–X hexagonal quasi-2D lattice that is covalently bonded, which is further confirmed by the ELF analysis described in the following sections [34, 65].

The structural integrity of the host is less susceptible to impurities commonly found in carbon-based graphite structures [66]. The layered $CrTe_2$ nanostructure has been prepared using a synthesis method involving cation exchange where the bulk $Cr_2Te_6$ non-layered structure is transformed into layered $CrTe_2$ by injecting a Cr precursor [67]. Furthermore, various methods including the solid-state reaction and the self-flux method have been used to synthesize the layered $CrTe_2$ structures for a variety of applications [66–69]. The sandwich structure height is 3.33 Å, the distance between the neighboring chalcogen atoms (X–X) and neighboring metal atoms (M–M) is 3.86 Å, the distance between the neighboring transition metal and chalcogen atoms (M–X) is 2.48 Å, the interlayer distance is 3.01 Å, and the angle between (X–M–X) atoms is 95.12° as per agreement with the literature [43].

### 3.2 | Dynamic Stability

Phonon dispersion curves are used to test the dynamical stability of structures and analyze the phonon spectra along high symmetry points in the Brillouin zone. The phonon band structure sheds light on the vibrational behavior of atoms in the lattice, which directly influences its kinetic stability. Figure 2 shows the calculated phonon curves of $CrTe_2$, which illustrates the absence of any negative frequencies and thus points to the dynamic stability of the material. The formation energy of host $CrTe_2$ calculated by Equation (1) appeared exothermically favorable, which indicates its structural stability and suitability for use as an anode material.

### 3.3 | Electronic Properties of Pure $CrTe_2$

The electronic properties are known to provide important information on the potential of the materials for use as electrodes in the batteries. The calculated band structure and density of states (DOS) of $CrTe_2$ are shown in Figure 3a,b, respectively, which illustrate the metallic nature of the material. Figure 3b delves deeper into this metallic character by showcasing the partial density of states (P-DOS), which reveal the contributions of Cr-3d and Te-5p states to the electronic character of $CrTe_2$ near the Fermi level. The involvement of both Cr and Te orbitals in these states exhibits their collaborative role in the metallic behavior of the material. This represents the absence of a band gap and the cohesive interplay of Cr and Te orbitals proximate to the Fermi level. These factors significantly enhance the electronic conductivity within $CrTe_2$, elucidating its potential efficacy as an anode material.

### 3.4 | Electron Localization Function (ELF)

To further investigate the electronic behavior of the anode material and to determine the chemical bonding of the host structure the ELF based on surface charge integral calculations is frequently used [70]. A value of 0 indicates delocalization, whereas 1 signifies the localization of electrons [71]. The ELF value of around 0.5 indicates electron delocalization typically observed in the case of metallic bonding, whereas higher ELF values indicate significant electron localization, which usually points to electron sharing between atoms that is typically observed for covalent bonding. The ionic bonding, characterized by a lower ELF value, indicates robust electron localization from electron transfer between atoms. The ELF of the host $CrTe_2$ is shown in Figure 2b according to which the localization appears around Te atoms, delocalization is found around Cr atoms, and a metallic bond Cr–Te is obvious.

### 3.5 | Hirshfeld Charge Analysis

Hirschfeld charge analysis helps to investigate the charge transfer between intercalated atoms and the host structure, which is critical for understanding the electrochemical operation of a battery. Figure 4 gives the calculated Hirsheld charges on atoms of the host before and intercalation of Li, Mg, and Al. The positive (negative) charge is represented by blue (red) color to characterize the donor (acceptor) atoms. In the case of pure

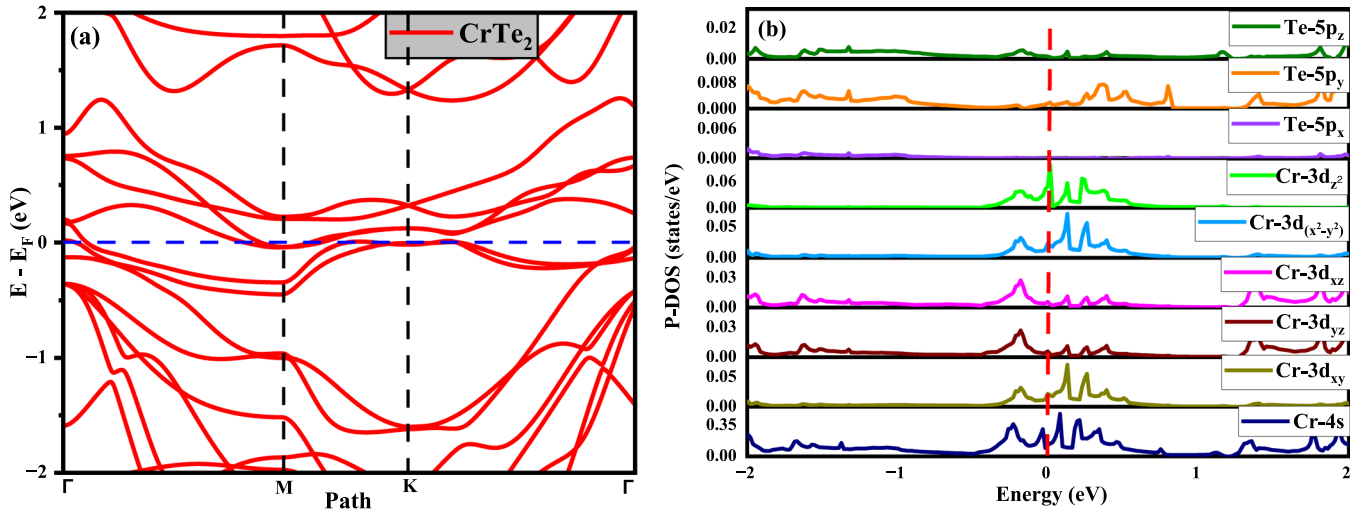


**FIGURE 3** | The calculated electronic properties. (a) Band structure of $CrTe_2$. The Fermi level is set at 0 eV. (b) Partial density of states (P-DOS) of $CrTe_2$. The P-DOS for Cr-3d and Te-5p display states as a function of energy in electron volts (eV).

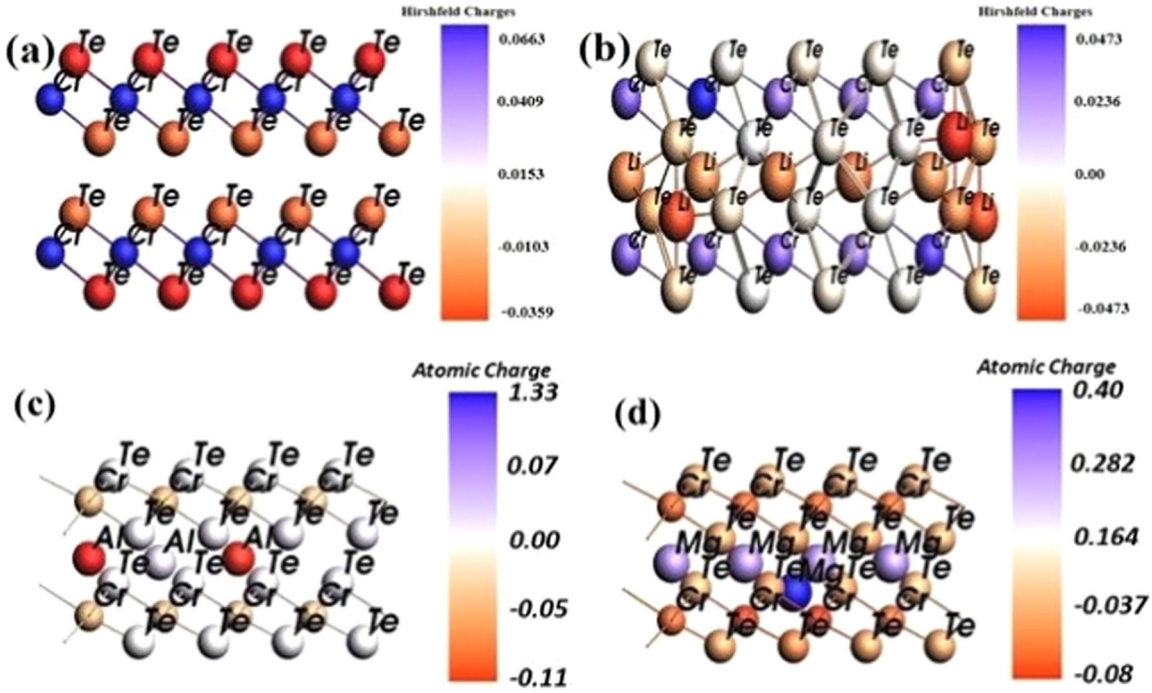


**FIGURE 4** | The calculated Hirshfeld charges of (a) pure $CrTe_2$, (b) Li-intercalated $CrTe_2$, (c) Al-intercalated $CrTe_2$, and (d) Mg-intercalated $CrTe_2$.

$CrTe_2$, Cr atoms appeared as donors, whereas Te acted as acceptor. The sketch of the Li-intercalated structure given in Figure 4b indicates a shift of small charge on Li atoms preferentially from Te atoms. In the case of Al intercalation given in Figure 4c, the shift of charge from both host atoms to Al atoms is observed. Similarly, in the case of Mg intercalation, Figure 4d indicates a transfer of charge from Mg to host atoms.

### 3.6 | Favorable Intercalation Sites

The determination of feasible sites for intercalation is an important step in understanding the process of intercalation in the host material [72, 73]. The energy profiling of the structure was carried out by placing metal atoms at different symmetry places in $CrTe_2$ layers. The negative values of intercalation energy confirm the reaction's exothermic nature, which demonstrates the host's feasibility as an anode. Equation (2) was used to calculate the intercalation energy in such a way that the more negative value of the intercalation energy points to the more favorable site to host the metal atoms [51]. In the case of LIB, the B2 site in the host structure indicates an energy of –0.89 eV as the most exothermic site because it is located near the Te atom, which has more electron affinity than Cr, as shown in Figure 5a.

Similarly, in the case of MIB and AIB, S1 and H1 sites in the host structure are the most exothermic sites with corresponding energy values of –1.99 and –1.87 eV, as shown in Figure 5b,c, respectively. The energy values calculated using the mentioned

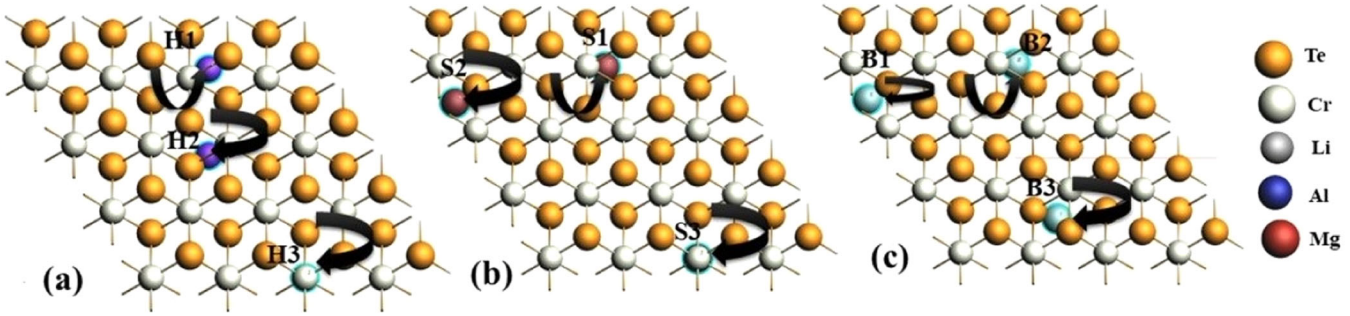


**FIGURE 5** | Favorable interstitial sites for (a) aluminum intercalation, (b) magnesium intercalation, and (c) lithium intercalation in the host $CrTe_2$.

**TABLE 1** | Intercalation energy (eV) of host $CrTe_2$ on the three favorable intercalation sites up to $X_x$ ($X$ = Li, Mg, and Al) where $x = 1$, 2, and 3.

| H1 | H2 | H3 |
|---|---|---|
| −1.87 | −1.55 | −1.71 |
| **S1** | **S2** | **S3** |
| −1.99 | −1.85 | −1.77 |
| **B1** | **B2** | **B3** |
| −0.89 | −0.63 | −0.47 |

sites are described in Table 1. The site offering the most negative intercalation energy is considered the most stable intercalation site to accommodate metal atoms in the host structure.

### 3.7 | The Intercalation Energy

We evaluated the adsorption energy of all $X$ atoms with the host structure (where $X$ represents three types of atoms Li, Mg, and Al). Lithium offers monovalent, Mg gives divalent, and Al presents trivalent oxidation states whose intercalation in the host is studied to understand the reaction dynamics between the embedded atom and the host by taking into account the exothermic (favorable) or endothermic (unfavorable) conditions. The concentration of $X$ atoms in the host structure steadily increases, and the adsorption energy is calculated using Equation (1). The reaction is feasible until the energy stays negative. However, after a certain saturation stage, the energy may turn positive, which indicates that the reaction is no longer advantageous to host the further $X$ atoms.

To begin, the Li intercalation energy in the host material is determined by inserting sequentially increasing the number of Li atoms in the host structure. The computed lithiation energy using Equation (2) indicates that the process stays exothermic until 20 Li atoms are intercalated into the host, as shown in Figure 7. The insertion of 21st atom (with $x = 21$) into the host structure turned the reaction into an endothermic condition.

Furthermore, Mg atoms are intercalated in the host structure, and the magnetization energy is computed using Equation (1). The process stays exothermic up to the insertion of fifth Mg atom, as shown in Figure 7, which shows the optimized structure of the host with intercalation of one Mg, three Mg, and five Mg atoms.

During the cation storage process in $CrTe_2$, the following reactions are proposed for lithium and other cations (like Mg and Al):

$$CrTe_2 + 6Li^+ \leftrightarrow Cr + 2Li_2Te_2$$

In this reaction, the chromium in $CrTe_2$ is reduced, which means that it gains electrons and is converted to elemental chromium (Cr). The tellurium in $CrTe_2$ is oxidized, reacting with lithium ions to form lithium telluride ($Li_2Te$). Each lithium atom donates an electron in the process.

Oxidation half-reaction:

$$Te^{-2} \rightarrow Li_2Te + 2e^-$$

Reduction half-reaction:

$$Cr^{+4} + 6e^- \rightarrow Cr$$

The redox reaction of $CrTe_2$ with magnesium can be represented as follows:

$$CrTe_2 + 3Mg \rightarrow Cr + 2Mg_2Te$$

In this reaction, chromium in $CrTe_2$ is reduced, gaining electrons to form elemental Cr. Tellurium in $CrTe_2$ is oxidized, reacting with magnesium to form magnesium telluride ($Mg_2Te$). Each magnesium atom donates electrons during this process.

Oxidation half-reaction:

$$Te^{-2} \rightarrow Mg_2Te + 2e^-$$

Reduction half-reaction:

$$Cr^{+4} + 6e^- \rightarrow Cr$$

This redox reaction illustrates the interaction of magnesium with $CrTe_2$, highlighting the reduction of chromium and the formation of $Mg_2Te$.

The redox reaction of $CrTe_2$ with aluminum can be represented as follows:

$$CrTe_2 + 2Al \rightarrow Cr + 2Al_2Te_3$$

In this reaction, chromium in $CrTe_2$ is reduced, gaining electrons to form elemental Cr. Tellurium in $CrTe_2$ is oxidized, reacting with aluminum to form aluminum telluride ($Al_2Te_3$). Each aluminum atom donates electrons in this process.

Oxidation half-reaction:

$$Te^{-2} \rightarrow Al_2Te_3 + 2e^-$$

Reduction half-reaction:

$$Cr^{+4} + 6e^- \rightarrow Cr$$

This redox reaction demonstrates aluminum interacts with $CrTe_2$, highlighting the reduction of chromium and the formation of $Al_2Te_3$. As we are dealing with supercells, the intercalation of metal atoms increases accordingly.

Lastly, Al atoms were gradually added in the host $CrTe_2$ as shown in Figure 6, which illustrates an optimized host structure with intercalation of one, two, and three Al atoms. The interaction of Al atoms in the host stays exothermic until three Al atoms are intercalated, as shown in Figure 7.

### 3.8 | Storage Capacity

The storage capacity of the anode in multivalent ion batteries is primarily determined by the amount of metal atoms that can be stored in the anode material per unit weight. The structure was fully optimized by allowing the reaction between the metal atoms and $CrTe_2$ layers to let the atoms settle into a stable position. The concentration of metal atoms in the host was gradually raised to compute the intercalation energy using Equation (2), to determine the nature of the reaction. The interlayer separation depicts minor changes as the concentration of metal atoms increases, indicating the stability of the host structure that can maintain its volume. The theoretical capacity of $CrTe_2$ as an anode material in LIBs is determined using Equation (3). The reaction remains exothermic up to the intercalation of 20 lithium atoms within the host structure. The calculated theoretical capacity is 1745 mAh $g^{-1}$, as shown in Figure 8a, which is the highest among all the studied monovalent and multivalent ion batteries. For MIBs, the capacity of $CrTe_2$ is measured using Equation (3) with the intercalation of five magnesium ions, resulting in a capacity of 872 mAh $g^{-1}$, as illustrated in Figure 8b. For AIBs, the capacity is determined using Equation (3) with the intercalation of three aluminum ions, resulting in a capacity of 785 mAh $g^{-1}$, as shown in Figure 8c. This is the lowest capacity of $CrTe_2$ as an anode material among all the considered batteries. The calculated parameters and comparison with the reported values are listed in Table 2.

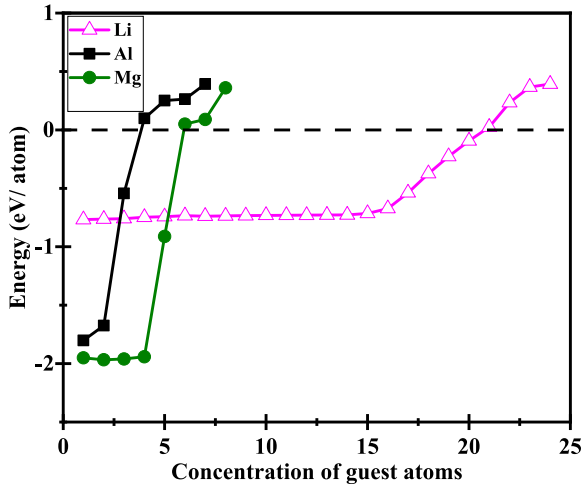


**FIGURE 7** | The intercalation energy of the host $CrTe_2$ as a function of concentration of Li, Mg, and Al. The dashed horizontal line separates the exothermic region (below 0) and endothermic region (above 0).

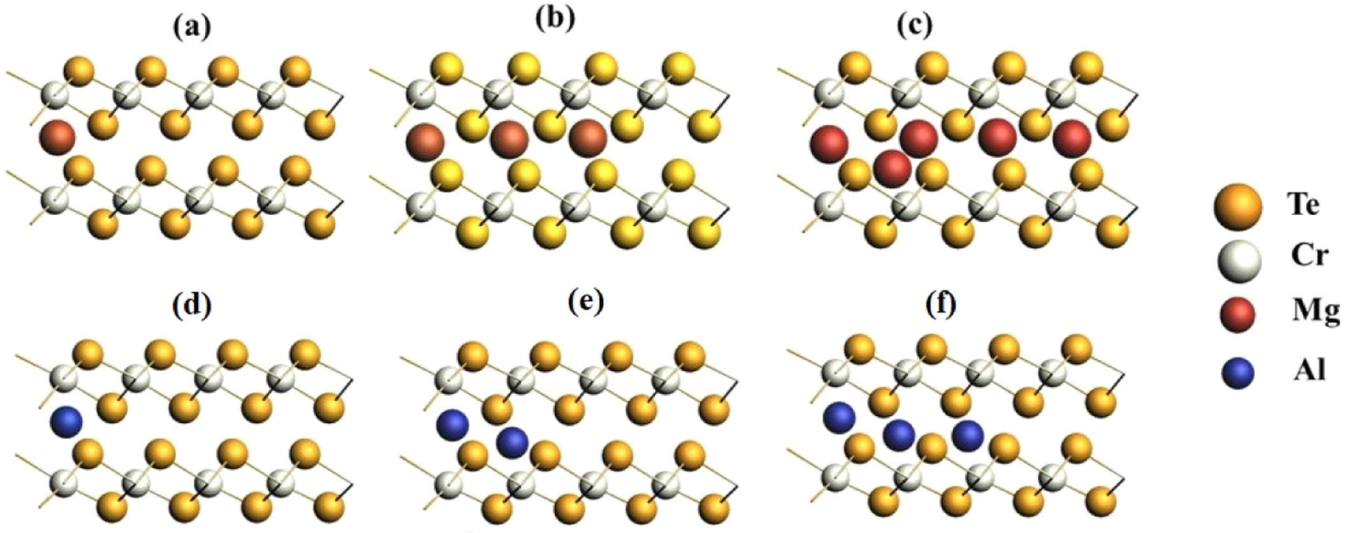


**FIGURE 6** | The optimized structure of $CrTe_2$ after incalation of (a) one Mg, (b) three Mg, (c) five Mg, (d) one Al, (e) two Al, and (f) three Al atoms.

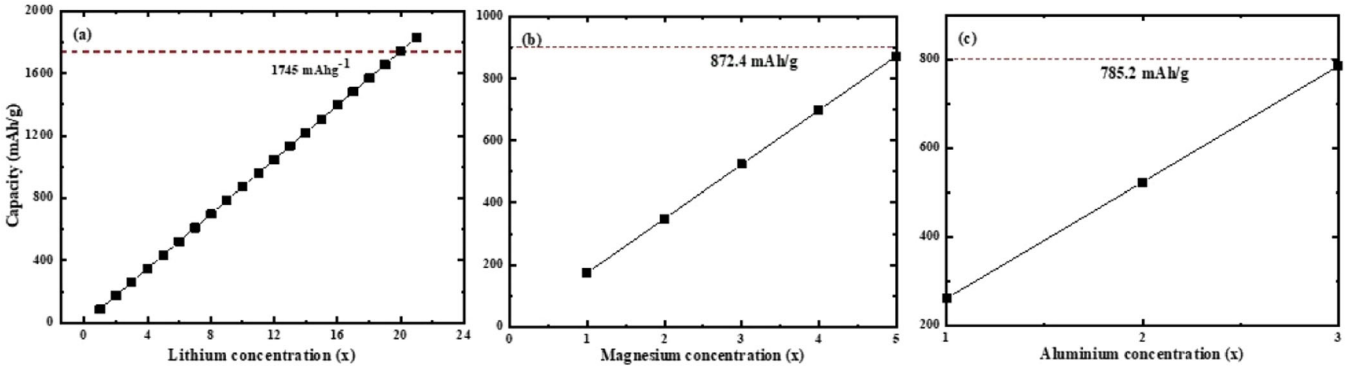


**FIGURE 8** | The calculated storage capacity of host $CrTe_2$ for (a) Li-ion batteries, (b) Mg-ion batteries, and (c) Al-ion batteries.

**TABLE 2** | The comparison of characteristics of $CrTe_2$ with reported anode materials.

| Anode materials | Theoretical capacity (mAh $g^{-1}$) | Diffusion barrier (eV) | OCV (V) | Reference |
|---|---|---|---|---|
| $CrTe_2$ (LIBs) | 1745 | 0.26 | 0.76–0.12 | This work |
| $CrTe_2$ (MIBs) | 872 | 0.55 | 0.97–0.42 | This work |
| $CrTe_2$ (AIBs) | 785 | 0.42 | 0.62–0.17 | This work |
| $LiC_6$ (Graphite) (LIBs) | 372 | 0.22–0.40 | 1.8 | [74] |
| $Li_2C_6$ (Bilayer graphene) (LIBs) | 744 | — | 0.4–0.6 | [75] |
| Si (LIBs) | 4200 | 0.58 | — | [76] |
| g-$CSi_2$ (Siligraphene) (LIBs) | 1286 | — | — | [77] |
| $Si_3N$ (LIBs) | 1772 | 0.24 | 0.15–0.90 | [78] |
| P–$Bi_3Sn_2$ electrode MIBs | 301 | | 0–0.8 | [79] |
| Micronized bulk $Mg_2Sn$ anode MIBs | 270 | — | — | [80] |
| Nanostructured Sn–Sb alloys MIBs | 270 | — | 0–0.8 | [81] |
| $B_2C$ (MIBs) | 3187.55 | 0.91 | 0.46 | [82] |

### 3.9 | Voltage Profile

The OCV is a crucial parameter that describes the magnitude of the driving forces required to achieve equilibrium between the cathode and anode [54]. The calculation of the voltage profile of host structures helps to estimate the electrochemical performance of metal-ion batteries [83]. The OCV plays a crucial role in predicting a battery's state of charge, enabling users and battery management systems to accurately estimate the remaining capacity. Moreover, OCV is essential in determining the voltage profile and overall voltage characteristics of the battery during both the charging and discharging phases. The open-circuit potential for the studied batteries is calculated using Equation (4). Figure 9a illustrates the voltage profile of $CrTe_2$ for LIBs, which shows a maximum value of 0.76 V, representing the second-highest value. The voltage profile for MIBs is shown in Figure 9b, with a peak value of 0.97 V, the highest among all the considered batteries. The voltage profile for AIBs is shown in Figure 9c, with a value of 0.62 V, the lowest among all the considered batteries.

### 3.10 | Diffusion Paths of Metal Atoms

The CI-NEB method is used to calculate the diffusion barrier and lowest energy route for the diffusion of metal atoms in the host structure. The method divides the reactant and product states of chemical reactions into intermediate states or images. The images were connected by an elastic band, which nudged along the reaction pathway to find the lowest energy path between the two states. The NEB calculation provides the diffusion energy barrier that is inversely proportional to the diffusion rate and gives us valuable information about the battery's charging process. The energy needed for metal atoms to migrate between the layers of the host structure is crucial for the charging efficiency of multivalent ion batteries and is greatly influenced by the transition barrier. Different transition pathways were considered in our simulation, as illustrated in Figure 10. The first migration path of Li within $CrTe_2$ entails passage from the middle hexagonal ring on the upper layer to the middle of the hexagonal ring on the lower layer along the *y*-axis. The energy barrier corresponding to this path appeared at 0.26 eV, as

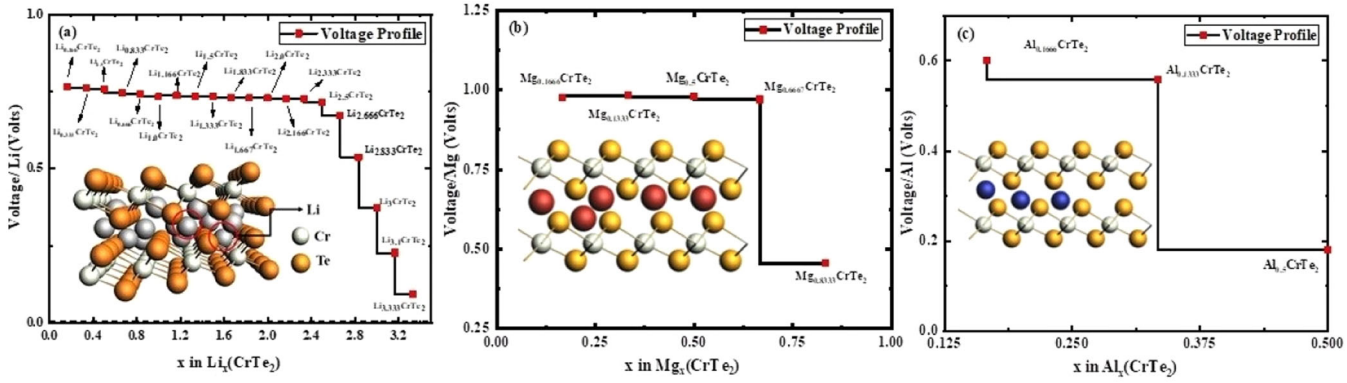


**FIGURE 9** | The voltage profiling of the host $CrTe_2$ for (a) Li-ion battery, (b) Mg-ion battery, and (a) Al-ion battery.

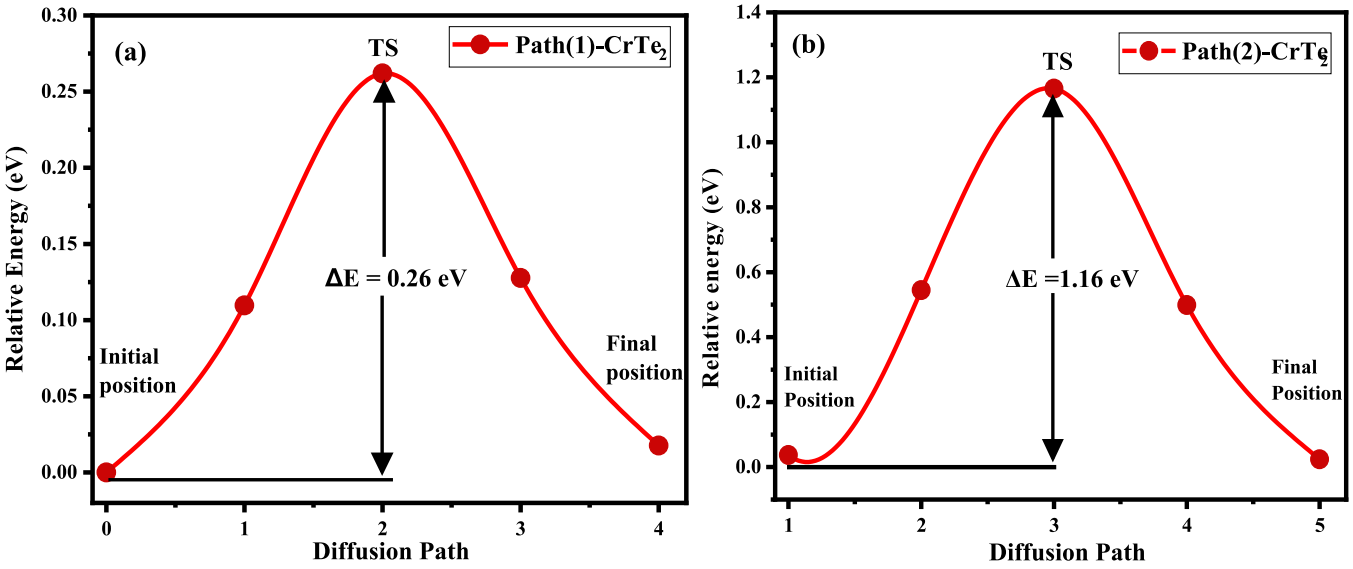


**FIGURE 10** | The Li migration paths within the host $CrTe_2$ (a) along path 1 relative energy plot during the diffusion between initial and final position with the energy barrier of 0.23 eV, and (b) relative energy graph between initial and final position during the diffusion with the energy barrier of 1.16 eV along path 2.

illustrated in Figure 10a. It is comparable with commercially used anode material graphite (0.22–0.40 eV) and $Si_3N$ (~0.24 eV). This transition pathway is suitable for lithiation within $CrTe_2$ [74, 78]. When the concentration of lithium is lower, the highly favorable and stable site is the center of the hexagonal ring. The bridging between two hexagonal rings creates the least energy needed for Li to diffuse into a stable position. In this pathway, the interacting Li atom is located near the Te atom in $CrTe_2$. The lithium atom transfers its charge to the tellurium atom, as confirmed by Hirshfeld charge analysis. The second migration path from left to right along the *x*-axis diffusion of Li within $CrTe_2$ has an energy barrier of 1.16 eV, as shown in Figure 10b. Notably, compared to all other pathways, Al has the lowest energy barrier on this path.

For the Mg diffusion in the host $CrTe_2$, two pathways are investigated. The diffusion channel of Mg into the host structure, with an energy barrier of 0.55 eV for diffusion from left to right along the *x*-axis, is depicted in Figure 11a, which is comparable to the $MoS_2$ (0.57 eV) [84]. The diffusion of magnesium from the top to bottom ring is shown in Figure 11b, which corresponds to an energy barrier of 0.95 eV that is comparable to that of $B_2C$ [82].

The diffusion of Al in the host $CrTe_2$ is also studied for the two pathways using Cl-NEB. The diffusion channel of Al in the host structure is depicted in Figure 12a, where an *x*-axis energy barrier of 0.42 eV is obtained. In contrast, in the case of Al diffusion from the top to the bottom rings, as shown in Figure 12b, a barrier of 1.33 eV is encountered.

### 3.11 | Current Voltage (IV) Characteristics of $CrTe_2$

To understand the role of electronic interactions in solid electrolyte interphase (SEI) formation, DFT-GF electron transport calculations are carried out for the pure and Li/Mg/Li interacted structures as shown in Figure 13. The circuit showing two gold electrodes acting as leads to provide voltage to the host material is given in Figure 14. Figure 14a represents the pure $CrTe_2$, Figure 14b represents the Li-intercalated $CrTe_2$, Figure 14c illustrates Mg intercalated $CrTe_2$, and Figure 14d demonstrates Al-intercalated $CrTe_2$. We are concerned with the electron flow that results from positive voltages; hence, the IV characteristics

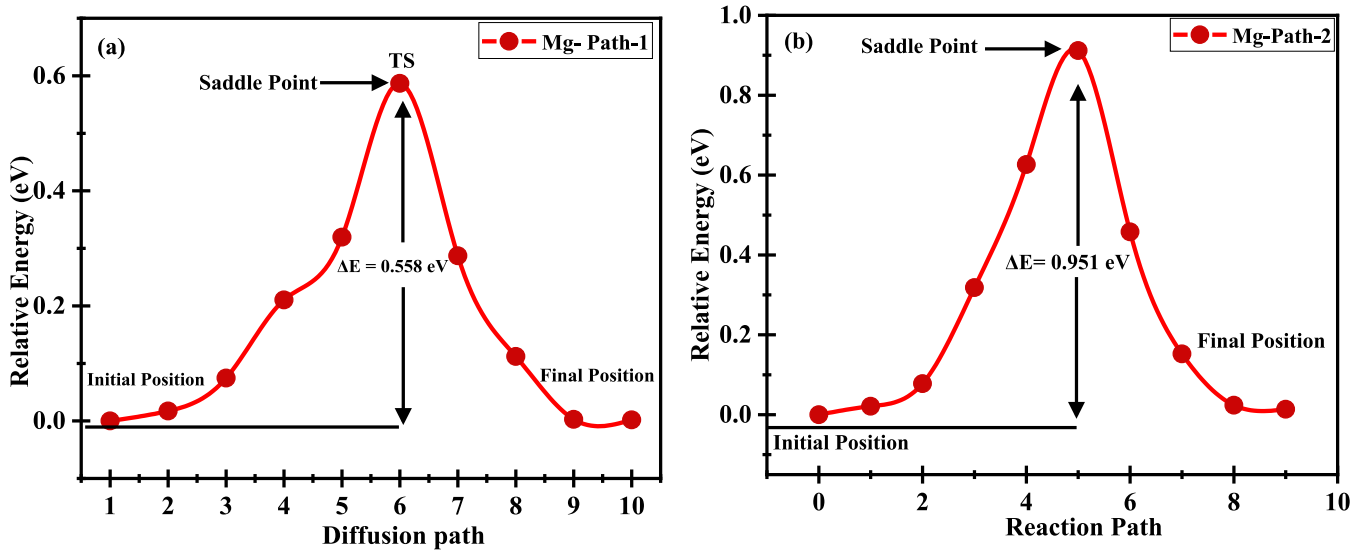


**FIGURE 11** | The Mg migration paths within the host $CrTe_2$ (a) along path 1 relative energy plot during the diffusion between initial and final position with the energy barrier of 0.6 eV, and (b) relative energy graph between initial and final position during the diffusion with the energy barrier of 0.95 eV along path 2.

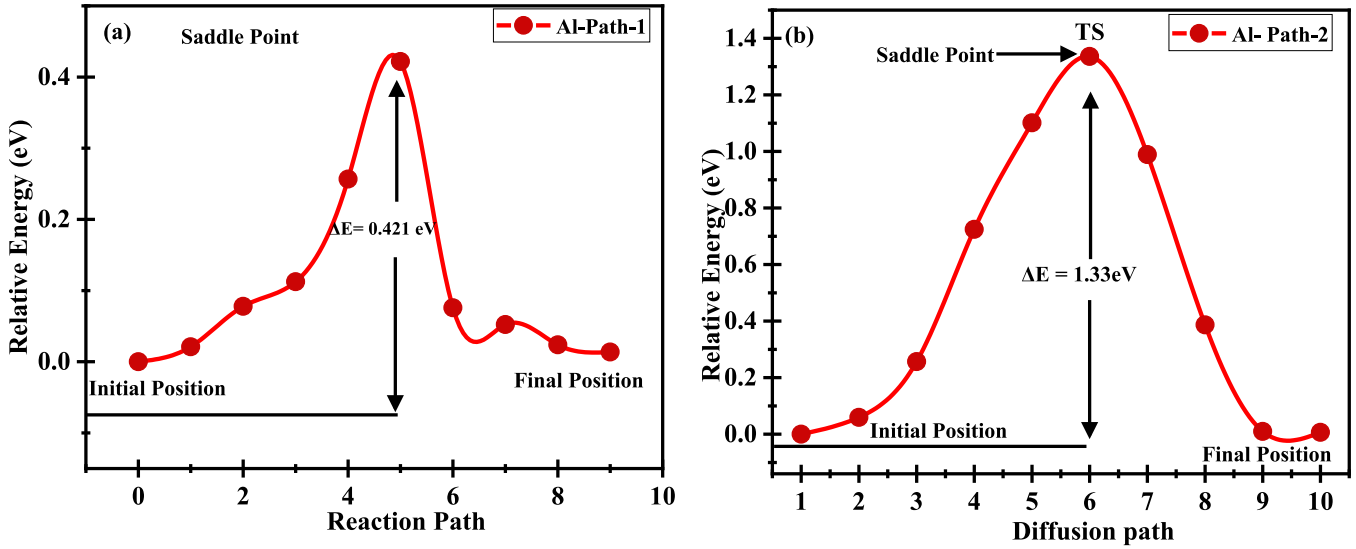


**FIGURE 12** | The Al migration paths within the host $CrTe_2$ (a) along path 1 relative energy plot during the diffusion between initial and final position with the energy barrier of 0.42 eV, and (b) relative energy graph between initial and final position during the diffusion with the energy barrier of 1.33 eV along path 2.

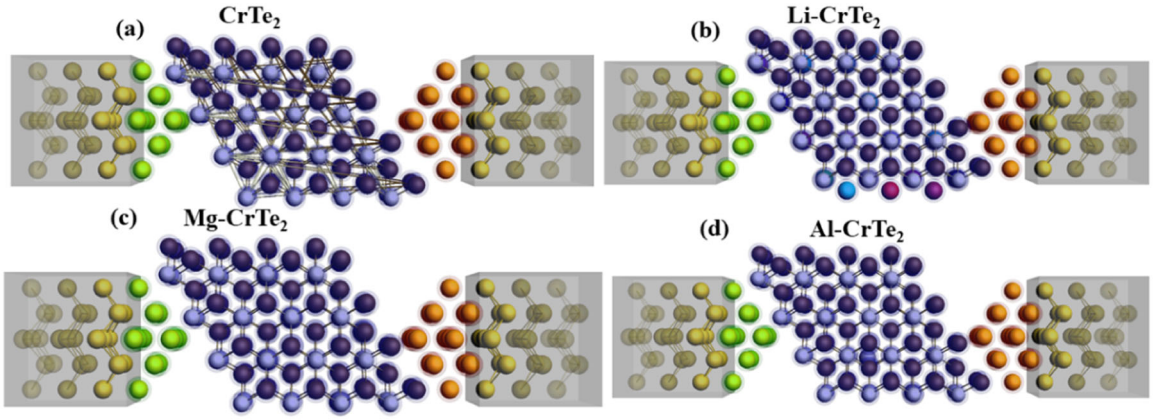


**FIGURE 13** | The view of NEGF setup of (a) pure $CrTe_2$, (b) Li-intercalated $CrTe_2$, (c) Mg-intercalated $CrTe_2$, and (d) Al-intercalated $CrTe_2$. The proposed anode material is placed between gold leads.

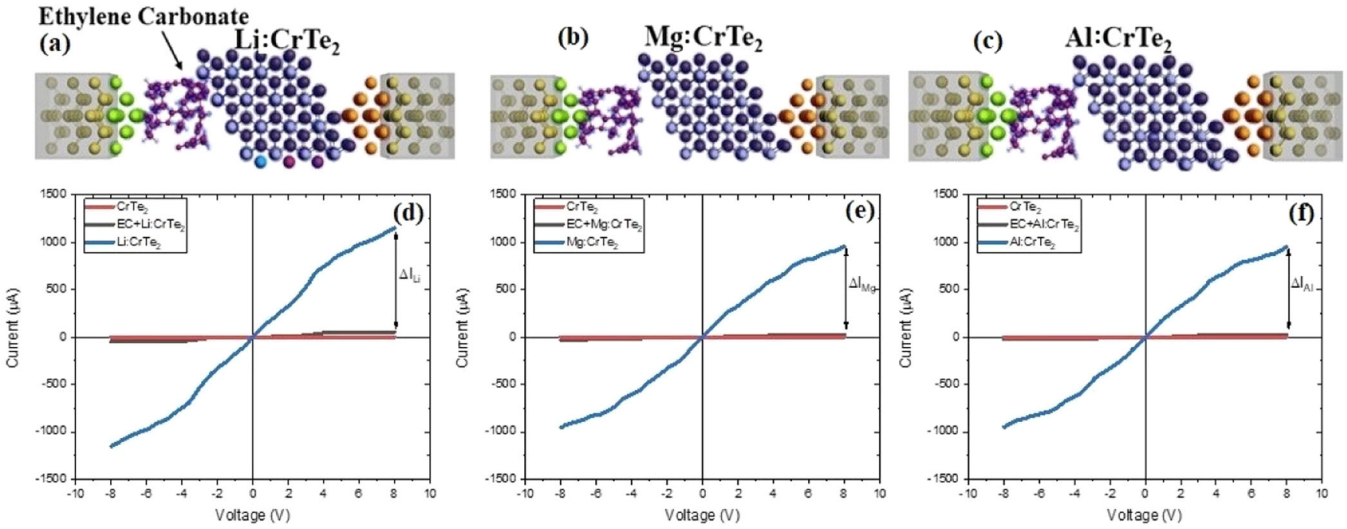


**FIGURE 14** | The view of NEGF setup where ethylene carbonate (EC) electrolyte is placed between gold lead and battery anode in the form of (a) Li-intercalated $CrTe_2$, (b) Mg-intercalated $CrTe_2$, and (c) Al-intercalated $CrTe_2$. The current–voltage (IV) characteristics showing (d) comparison of IV curves of pure $CrTe_2$, Li-intercalated $CrTe_2$, and EC + Li-intercalated $CrTe_2$; (e) comparison of IV curves of pure $CrTe_2$, Mg-intercalated $CrTe_2$, and EC + Mg-intercalated $CrTe_2$; (f) comparison of IV curves of pure $CrTe_2$, Al-intercalated $CrTe_2$, and EC + Al-intercalated $CrTe_2$. The change in current with and without EC is shown.

are only computed for applied voltages in the range of −5 to +5 V. Figure 14d–f represents that the pure $CrTe_2$ has the minimum value of current 0.0009 μA, which is observed notably rise to 955 and 950 μA when the respective Mg and Al atoms are intercalated in the host material.

Furthermore, we placed the ethylene carbonate (EC) as electrolyte near the anode material $CrTe_2$ to investigate the transportation of electrons, as shown in Figure 14a–c for Li, Mg, and Al-intercalated $CrTe_2$, respectively. The IV curves shown in Figure 14d–f point to (i) a notable increase in current when intercalation of the metal atoms takes place in the host, and (ii) a significant decrease in the current after the introduction of the EC electrolyte in all studied cases. The decrease in the current owes to the formation of the SEI layer on the anode after the application of the external voltage. SEI development causes capacity loss in silicon anodes, which significantly impedes their practical use in the next generation of high-energy LIBs [85].

The analysis of IV curves of the intercalated host points to a reduction in the current, which takes place in descending order of $I_{Li:CrTe_2} < I_{Mg:CrTe_2} < I_{Al:CrTe_2}$ due to reactions involving electron transfer. The notable reduction from monovalent Li case of multivalent Mg and Al atoms. In the early stage, the formation of SEI takes place on the surface of the anode when electrolyte EC is reduced by donating electrons [76]. The application of applied voltage introduces a current comprising electrons donated by EC and metal ions to facilitate the reactions involved in SEI formation. The comparison of the systems with and without the electrolyte clearly indicates the significant decrease in current (indicated by $\Delta I_X$) upon the formation of the SEI components. In the case of monovalent Li-intercalated anode, the value of decrease in current $\Delta I_{Li}$ is 1101 μA, whereas the decrease in current for multivalent Mg- and Al-intercalated anodes, the values of $\Delta I_{Mg}$ and $\Delta I_{Al}$ are found at 927.5 μA and 928 μA, respectively. The results predict that the simultaneous transfer of electrons from EC and $X^{n+}$ ions from the intercalated anode to form SEI is dependent on the valance status of the $X$ atom. The provision of a higher number of electrons in the formation of SEI in the case of multivalent ion batteries will facilitate the quicker formation of stable SEI, which is a requirement to develop cost-effective and efficient metal-ion batteries [77, 86–88].

## 4 | Summary

In summary, our study provides compelling evidence that two-dimensional (2D) puckered chromium ditelluride ($CrTe_2$) holds significant promise as an anode material for multivalent metal-ion batteries operating via lithium (Li), magnesium (Mg), and aluminum (Al) ions. Through DFT calculations, we comprehensively investigated the stability, structural properties, and electronic characteristics of $CrTe_2$, alongside its diffusion barriers, storage capacities, OCV, and adsorption sites. The exothermic interactions of $CrTe_2$ with Li, Mg, and Al ions confirmed its suitability for intercalation processes in both monovalent and multivalent ion batteries. The calculated values of storage capacities are notably high with values of 1745 mAh $g^{-1}$ for LIBs, 872 mAh $g^{-1}$ for MIBs, and 785 mAh $g^{-1}$ for AIBs. The OCVs of $CrTe_2$ are 0.76 V for Li, 0.97 V for Mg, and 0.62 V for Al. Furthermore, the low diffusion barriers of 0.26 eV for LIBs, 0.55 eV for MIBs, and 0.42 eV for AIBs indicate the potential for rapid charging capabilities due to efficient ion movement. We investigate the electron transport properties in a few finite models of the host material using a combined DFT and Green's function method (DFT-GF). When compared to systems without SEI components, it is evident in every instance that the current is significantly decreased with the installation of SEI components These findings suggest that $CrTe_2$ could be a potential anode material in the development

of high-performance metal-ion batteries. Its ability to support fast charging rates, combined with substantial storage capacity and favorable voltage profiles, highlights the feasibility of $CrTe_2$ in advancing the technology of multivalent metal-ion batteries.


### Acknowledgments

The author from ADU acknowledges financial support from Abu Dhabi University's Office of Research and Sponsored Programs (Grant numbers 19300638 and 19300791) and the authors sincerely appreciate funding from Researchers Supporting Project number (RSP2025R58), King Saud University, Riyadh, Saudi Arabia.


### Ethics Statement

The authors have nothing to report.

### Conflicts of Interest

The authors declare no conflicts of interest.

### Data Availability Statement

The data that support the findings of this study are available on request from the corresponding author. The data are not publicly available due to privacy or ethical restrictions.

### References


1. A. Q. Al-Shetwi, "Sustainable Development of Renewable Energy Integrated Power Sector: Trends, Environmental Impacts, and Recent Challenges," *Science of the Total Environment* 822 (2022): 153645.

2. W. A. Salah, M. Abuhelwa, and M. J. Bashir, "The Key Role of Sustainable Renewable Energy Technologies in Facing Shortage of Energy Supplies in Palestine: Current Practice and Future Potential," *Journal of Cleaner Production* 293 (2021): 125348.

3. J. Munyaneza, M. Wakeel, and B. Chen, "Overview of Rwanda Energy Sector: From Energy Shortage to Sufficiency," *Energy Procedia* 104 (2016): 215–220.

4. J. Xiong, Z. Zhao, D. Liu, and L. He, "Direct Lithium Extraction From Raw Brine by Chemical Redox Method With $LiFePO_4/FePO_4$ Materials," *Separation and Purification Technology* 290 (2022): 120789.

5. M. M. Amaral, S. B. Mujib, H. Zanin, and G. Singh, "A Perspective on Silicon-Based Polymer-Derived Ceramics Materials for Beyond Lithium-Ion Batteries," *Journal of Physics: Materials* 6, no. 2 (2023): 021001.

6. S. Wu, R. Xu, M. Lu, et al., "Graphene-Containing Nanomaterials for Lithium-Ion Batteries," *Advanced Energy Materials* 5, no. 21 (2015): 1500400.

7. D. S. Jang, S. Yun, S. H. Hong, W. Cho, and Y. Kim, "Performance Characteristics of a Novel Heat Pipe-Assisted Liquid Cooling System for the Thermal Management of Lithium-Ion Batteries," *Energy Conversion and Management* 251 (2022): 115001.

8. H. Wang, H. Xu, Z. Zhang, et al., "Fire and Explosion Characteristics of Vent Gas From Lithium-Ion Batteries After Thermal Runaway: A Comparative Study," *eTransportation* 13 (2022): 100190.

9. H. Jia, Y. Xu, L. Zou, et al., "Sulfone-Based Electrolytes for High Energy Density Lithium-Ion Batteries," *Journal of Power Sources* 527 (2022): 231171.

10. X. Han, M. Ouyang, L. Lu, J. Li, Y. Zheng, and Z. Li, "A Comparative Study of Commercial Lithium Ion Battery Cycle Life in Electrical Vehicle: Aging Mechanism Identification," *Journal of Power Sources* 251 (2014): 38–54.

11. W. Cao, J. Zhang, and H. Li, "Batteries With High Theoretical Energy Densities," *Energy Storage Materials* 26 (2020): 46–55.

12. Y. Gao, Z. Pan, J. Sun, Z. Liu, and J. Wang, "High-Energy Batteries: Beyond Lithium-Ion and Their Long Road to Commercialisation," *Nano-Micro Letters* 14, no. 1 (2022): 94.

13. S.-M. Paek, E. Yoo, and I. Honma, "Enhanced Cyclic Performance and Lithium Storage Capacity of $SnO_2$/Graphene Nanoporous Electrodes With Three-Dimensionally Delaminated Flexible Structure," *Nano Letters* 9, no. 1 (2009): 72–75.

14. M. He, H. P. Zhou, G. Q. Ding, et al., "Theoretical-Limit Exceeded Capacity of the $N_2$ + $H_2$ Plasma Modified Graphite Anode Material," *Carbon* 146 (2019): 194–199.

15. L.-F. Cui, L. Hu, J. W. Choi, and Y. Cui, "Light-Weight Free-Standing Carbon Nanotube-Silicon Films for Anodes of Lithium Ion Batteries," *ACS Nano* 4, no. 7 (2010): 3671–3678.

16. M. Ge, J. Rong, X. Fang, and C. Zhou, "Porous Doped Silicon Nanowires for Lithium Ion Battery Anode With Long Cycle Life," *Nano Letters* 12, no. 5 (2012): 2318–2323.

17. S. W. Lee, M. T. McDowell, L. A. Berla, W. D. Nix, and Y. Cui, "Fracture of Crystalline Silicon Nanopillars During Electrochemical Lithium Insertion," *Proceedings of the National Academy of Sciences* 109, no. 11 (2012): 4080–4085.

18. S. Hussain, X. Yang, M. K. Aslam, et al., "Robust TiN Nanoparticles Polysulfide Anchor for Li–S Storage and Diffusion Pathways Using First Principle Calculations," *Chemical Engineering Journal* 391 (2020): 123595.

19. J. Wang, D. Kober, G. Shao, et al., "Stable Anodes for Lithium-Ion Batteries Based on Tin-Containing Silicon Oxycarbonitride Ceramic Nanocomposites," *Materials Today Energy* 26 (2022): 100989.

20. K. L. Ng, Z. Lu, Y. Wang, C. V. Singh, and G. Azimi, "Fundamental Insights Into Electrical and Transport Properties of Chloroaluminate Ionic Liquids for Aluminum-Ion Batteries," *Journal of Physical Chemistry C* 125, no. 28 (2021): 15145–15154.

21. J. Muldoon, C. B. Bucur, and T. Gregory, "Quest for Nonaqueous Multivalent Secondary Batteries: Magnesium and Beyond," *Chemical Reviews* 114, no. 23 (2014): 11683–11720.

22. S. Wang, Z. Yu, J. Tu, et al., "A Novel Aluminum-Ion Battery: $Al/AlCl_3$-[EMIm] $Cl/Ni_3S_2$@ Graphene," *Advanced Energy Materials* 6, no. 13 (2016): 1600137.

23. T. Cai, L. Zhao, H. Hu, et al., "Stable $CoSe_2$/Carbon Nanodice@ Reduced Graphene Oxide Composites for High-Performance Rechargeable Aluminum-Ion Batteries," *Energy & Environmental Science* 11, no. 9 (2018): 2341–2347.

24. R. Dong, T. Zhang, and X. Feng, "Interface-Assisted Synthesis of 2D Materials: Trend and Challenges," *Chemical Reviews* 118, no. 13 (2018): 6189–6235.

25. L. Peng, Y. Zhu, D. Chen, R. S. Ruoff, and G. Yu, "Two-Dimensional Materials for Beyond-Lithium-Ion Batteries," *Advanced Energy Materials* 6, no. 11 (2016): 1600025.

26. Y. Bahari, B. Mortazavi, A. Rajabpour, X. Zhuang, and T. Rabczuk, "Application of Two-Dimensional Materials as Anodes for Rechargeable Metal-Ion Batteries: A Comprehensive Perspective From Density Functional Theory Simulations," *Energy Storage Materials* 35 (2021): 203–282.

27. X. Feng, H. Fang, N. Wu, et al., "Review of Modification Strategies in Emerging Inorganic Solid-State Electrolytes for Lithium, Sodium, and Potassium Batteries," *Joule* 6, no. 3 (2022): 543–587.

28. T. Bashir, S. Zhou, S. Yang, et al., "Progress in 3D-MXene Electrodes for Lithium/Sodium/Potassium/Magnesium/Zinc/Aluminum-Ion Batteries," *Electrochemical Energy Reviews* 6, no. 1 (2023): 5.

29. M. Liang, L. Ma, B. Chen, et al., "Two Birds With One Stone: A NaCl-Assisted Strategy Toward $MoTe_2$ Nanosheets Nanoconfined in 3D

Porous Carbon Network for Sodium-Ion Battery Anode," *Energy Storage Materials* 47 (2022): 591–601.

30. M. R. Panda, R. Gangwar, D. Muthuraj, et al., "High Performance Lithium-Ion Batteries Using Layered 2H-$MoTe_2$ as Anode," *Small* 16, no. 38 (2020): 2002669.

31. A. McCreary, O. Kazakova, D. Jariwala, and Z. Y. Al Balushi, "An Outlook Into the Flat Land of 2D Materials Beyond Graphene: Synthesis, Properties and Device Applications," *2D Materials* 8, no. 1 (2020): 013001.

32. J. Si, Y. Sun, R. Qi, et al., "Deep Multiphase Conversion Derived From $NiTe_2$ Nanosheets With Preferred Kinetics for Highly Reversible Mild Aqueous Zinc–Tellurium Batteries," *Advanced Energy Materials* 14, no. 14 (2024): 2303982.

33. S. Ahmed, M. Alkhedher, M. Isa, and A. Majid, "First Principles Study of Layered $CrGeTe_3$ as Lithium Intercalation Compound," *Journal of the Electrochemical Society* 169, no. 4 (2022): 040557.

34. F. G. Aras, A. Yilmaz, H. G. Tasdelen, et al., "A Review on Recent Advances of Chemical Vapor Deposition Technique for Monolayer Transition Metal Dichalcogenides ($MX_2$: Mo, W; S, Se, Te)," *Materials Science in Semiconductor Processing* 148 (2022): 106829.

35. M. A. Aghamalyan, V. M. Aroutiounian, E. S. Mamasakhlisov, et al., "Adsorption of Hydrogen Peroxide on Two-Dimensional Transition Metal Chalcogenides," *Journal of Contemporary Physics (Armenian Academy of Sciences)* 57, no. 2 (2022): 170–173.

36. A. F. Wani, B. Rani, U. B. Sharopov, S. Dhiman, and K. Kaur, "Thermoelectric Investigation of Transition Metal Oxide $NiO_2$: A First Principles Study," *International Journal of Energy Research* 46, no. 6 (2022): 8527–8535.

37. N. Nitta and G. Yushin, "High-Capacity Anode Materials for Lithium-Ion Batteries: Choice of Elements and Structures for Active Particles," *Particle & Particle Systems Characterization* 31, no. 3 (2014): 317–336.

38. P. Phalswal, P. K. Khanna, H. G. Rubahn, and Y. K. Mishra, "Nanostructured Molybdenum Dichalcogenides: A Review," *Materials Advances* 3, no. 14 (2022): 5672–5697.

39. F. He, C. Tang, Y Liu, and H. Li, "Carbon-Coated $MoS_2$ Nanosheets@ CNTs-$Ti_3C_2$ Mxene Quaternary Composite With the Superior Rate Performance for Sodium-Ion Batteries," *Journal of Materials Science & Technology* 100 (2022): 101–109.

40. T. Wang, K. Yao, Y. Hua, E. G. Shankar, R. Shanthappa, and J. S. Yu, "Rational Design of MXene-$MoS_2$ Heterostructure With Rapid Ion Transport Rate as an Advanced Anode for Sodium-Ion Batteries," *Chemical Engineering Journal* 457 (2023): 141363.

41. Y. Ma and P. S. Hooda, "Chromium, Nickel and Cobalt," in *Trace Elements in Soils* (2010): 461–479.

42. L. Persichetti, F. Jardali, H. Vach, et al., "Van Der Waals Heteroepitaxy of Germanene Islands on Graphite," *Journal of Physical Chemistry Letters* 7, no. 16 (2016): 3246–3251.

43. C. Linares-Flores, M. Rojas-Poblete, R. Guajardo-Maturana, L. Velasquez, and E. Schott, "Design of New Porous Supramolecular Arrays From Flavyliums Derivative Linker: A Theoretical Assemble Toward Surface Properties," *Computational Materials Science* 204 (2022): 111202.

44. H.-Y. Yu, J. S. Wang, F. Y. Xie, et al., "A Stack-Guiding Unit Constructed 2D COF With Improved Charge Carrier Transport and Versatile Photocatalytic Functions," *Chemical Engineering Journal* 445 (2022): 136713.

45. M. B. Solanki, P. Patel, S. Shinde, B. B. Parekh, and M. Joshi, "Growth and Characterization of Lithium Chloride Doped KDP Crystals: A DFT and Experimental Approach," *Ferroelectrics* 571, no. 1 (2021): 1–25.

46. J. Dykes, K. Kappenman, and E. D. Nissen, "Using DNA Barcoding Methods to Identify Wild Huckleberry, *Vaccinium membranaceum*, as a Classroom Project," *American Biology Teacher* 84, no. 1 (2022): 40–44.

47. J. G. Brandenburg and S. Grimme, "Accurate Modeling of Organic Molecular Crystals by Dispersion-Corrected Density Functional Tight Binding (DFTB)," *Journal of Physical Chemistry Letters* 5, no. 11 (2014): 1785–1789.

48. V. M. Miriyala and J. Řezáč, "Description of Non-Covalent Interactions in SCC-DFTB Methods," *Journal of Computational Chemistry* 38, no. 10 (2017): 688–697.

49. S. Hirata, "Nonvanishing Quadrature Derivatives in the Analytical Gradients of Density Functional Energies in Crystals and Helices," *Molecular Physics* 121, no. 9–10 (2022): e2086500.

50. M. Medves, D. Toffoli, M. Stener, L. Sementa, and A. Fortunelli, "Coupling Between Plasmonic and Molecular Excitations: TDDFT Investigation of an Ag-Nanorod/BODIPY–Dye Interaction," *The Journal of Physical Chemistry A* 126, no. 35 (2022): 5890–5899.

51. L. Jin, J. Zheng, and J. P. Zheng, "Theoretically Quantifying the Effect of Pre-Lithiation on Energy Density of Li-Ion Batteries," *Journal of the Electrochemical Society* 168, no. 1 (2021): 010532.

52. J. Tian, R. Xiong, W. Shen, and F. Sun, "Electrode Ageing Estimation and Open Circuit Voltage Reconstruction for Lithium Ion Batteries," *Energy Storage Materials* 37 (2021): 283–295.

53. S. Ullah, P. A. Denis, and F. Sato, "First-Principles Study of Dual-Doped Graphene: Towards Promising Anode Materials for Li/Na-Ion Batteries," *New Journal of Chemistry* 42, no. 13 (2018): 10842–10851.

54. Y. Dong, W. Wei, X. Lv, B. Huang, and Y. Dai, "Semimetallic $Si_3C$ as a High Capacity Anode Material for Advanced Lithium Ion Batteries," *Applied Surface Science* 479 (2019): 519–524.

55. X. Zhang, C. Yang, Y. Pan, et al., "Monolayer GaS With High Ion Mobility and Capacity as a Promising Anode Battery Material," *Journal of Materials Chemistry A* 7, no. 23 (2019): 14042–14050.

56. W. Qin, W. C. Lu, X. Y. Xue, K. M. Ho, and C. Z. Wang, "Lithium Diffusion in Silicon Encapsulated With Graphene," *Nanomaterials* 11, no. 12 (2021): 3397.

57. D. Eriksson, M. Pearce, J. Gardner, R. D. Turner, and M. Poloczek, "Scalable Global Optimization via Local Bayesian Optimization," *Advances in Neural Information Processing Systems* 32 (2019): 1–12.

58. C. J. O. Verzijl and J. M. Thijssen, "DFT-Based Molecular Transport Implementation in ADF/BAND," *Journal of Physical Chemistry C* 116, no. 46 (2012): 24393–24412.

59. N. Agraït, A. L. Yeyati, and J. M. Van Ruitenbeek, "Quantum Properties of Atomic-Sized Conductors," *Physics Reports* 377, no. 2–3 (2003): 81–279.

60. L. Venkataraman, J. E. Klare, C. Nuckolls, M. S. Hybertsen, and M. L. Steigerwald, "Dependence of Single-Molecule Junction Conductance on Molecular Conformation," *Nature* 442, no. 7105 (2006): 904–907.

61. Y. Meir and N. S. Wingreen, "Landauer Formula for the Current Through an Interacting Electron Region," *Physical Review Letters* 68, no. 16 (1992): 2512–2515.

62. A. Arnold, F. Weigend, and F. Evers, "Quantum Chemistry Calculations for Molecules Coupled to Reservoirs: Formalism, Implementation, and Application to Benzenedithiol," *Journal of Chemical Physics* 126, no. 17 (2007): 174101.

63. D. C. Freitas, R. Weht, A. Sulpice, et al., "Ferromagnetism in Layered Metastable 1T-$CrTe_2$," *Journal of Physics: Condensed Matter* 27, no. 17 (2015): 176002.

64. S. Chai, X. Xiao, Y. Li, and C. An, "Graphene-Coated 1D MoTe2 Nanorods as Anode for Enhancing Lithium-Ion Battery Performance," *Chinese Journal of Structural Chemistry* 41, no. 8 (2022): 2208018–2208024.

65. Y. Zhao, X. Kong, M. J. Shearer, F. Ding, and S. Jin, "Chemical Etching of Screw Dislocated Transition Metal Dichalcogenides," *Nano Letters* 21, no. 18 (2021): 7815–7822.

66. Y. Liu, S. Kwon, G. J. de Coster, R. K. Lake, and M. R. Neupane, "Structural, Electronic, and Magnetic Properties of $CrTe_2$," *Physical Review Materials* 6, no. 8 (2022): 084004.

67. C. Wang, Q. Zou, Z. Cheng, et al., "Tailoring Atomic 1T Phase $CrTe_2$ for In Situ Fabrication," *Nanotechnology* 33, no. 8 (2021): 085302.

68. A. Purbawati, J. Coraux, J. Vogel, et al., "In-Plane Magnetic Domains and Néel-Like Domain Walls in Thin Flakes of the Room Temperature $CrTe_2$ Van Der Waals Ferromagnet," *ACS Applied Materials & Interfaces* 12, no. 27 (2020): 30702–30710.

69. X. Zhang, Q. Lu, W. Liu, et al., "Room-Temperature Intrinsic Ferromagnetism in Epitaxial $CrTe_2$ Ultrathin Films," *Nature Communications* 12, no. 1 (2021): 2492.

70. G. Mierzwa, A. J. Gordon, and S. Berski, "The Nature of Multiple Boron-Nitrogen Bonds Studied Using Electron Localization Function (ELF), Electron Density (AIM), and Natural Bond Orbital (NBO) Methods," *Journal of Molecular Modeling* 26 (2020): 136.

71. K. Koumpouras and J. A. Larsson, "Distinguishing Between Chemical Bonding and Physical Binding Using Electron Localization Function (ELF)," *Journal of Physics: Condensed Matter* 32, no. 31 (2020): 315502.

72. D. Yang, C. Zhang, J. J. Biendicho, et al., "ZnSe/N-Doped Carbon Nanoreactor With Multiple Adsorption Sites for Stable Lithium–Sulfur Batteries," *ACS Nano* 14, no. 11 (2020): 15492–15504.

73. J. Zhang, Y. F. Zhang, Y. Li, et al., "Defective BC2N as an Anode Material With Improved Performance for Lithium-Ion Batteries," *Journal of Physical Chemistry C* 125, no. 9 (2021): 4946–4954.

74. K. Persson, V. A. Sethuraman, L. J. Hardwick, et al., "Lithium Diffusion in Graphitic Carbon," *Journal of Physical Chemistry Letters* 1, no. 8 (2010): 1176–1180.

75. A. E. Galashev, O. R. Rakhmanova, and Y. P. Zaikov, "Defect Silicene and Graphene as Applied to the Anode of Lithium-Ion Batteries: Numerical Experiment," *Physics of the Solid State* 58 (2016): 1850–1857.

76. Y. Domi, H. Usui, K. Yamaguchi, S. Yodoya, and H. Sakaguchi, "Silicon-Based Anodes With Long Cycle Life for Lithium-Ion Batteries Achieved by Significant Suppression of Their Volume Expansion in Ionic-Liquid Electrolyte," *ACS Applied Materials & Interfaces* 11, no. 3 (2019): 2950–2960.

77. H. Wang, M. Wu, X. Lei, et al., "Siligraphene as a Promising Anode Material for Lithium-Ion Batteries Predicted From First-Principles Calculations," *Nano Energy* 49 (2018): 67–76.

78. H. Li, J. Hou, and D. Jiang, "2D $Si_3N$ as a Promising Anode Material for Li/Na-Ion Batteries From First-Principles Study," *Journal of Electronic Materials* 49 (2020): 4180–4185.

79. J. Niu, K. Yin, H. Gao, et al., "Composition-And Size-Modulated Porous Bismuth–Tin Biphase Alloys as Anodes for Advanced Magnesium Ion Batteries," *Nanoscale* 11, no. 32 (2019): 15279–15288.

80. D.-T. Nguyen and S.-W. Song, "Magnesium Stannide as a High-Capacity Anode for Magnesium-Ion Batteries," *Journal of Power Sources* 368 (2017): 11–17.

81. Y. Cheng, Y. Shao, L. R. Parent, et al., "Interface Promoted Reversible Mg Insertion in Nanostructured Tin–Antimony Alloys," *Advanced Materials* 27, no. 42 (2015): 6598–6605.

82. G. T. Kasprzak and A. P. Durajski, "Two-Dimensional $B_2C$ as a Potential Anode Material for Mg-Ion Batteries With Extremely High Theoretical Capacity," *Scientific Reports* 12, no. 1 (2022): 11460.

83. C. Zhang, Y. Jiao, T. He, et al., "Two-Dimensional $GeP_3$ as a High Capacity Electrode Material for Li-Ion Batteries," *Physical Chemistry Chemical Physics* 19, no. 38 (2017): 25886–25890.

84. J. Hu, W. Jin, Z. Tan, et al., "Potential Application of 2D Haeckelite $MoS_2$ as an Anode Material for Mg Ion Batteries," *Langmuir* 40 (2024): 19396–19403.

85. Q. Fang, S. Xu, X. Sha, et al., "Interfacial Degradation of Silicon Anodes in Pouch Cells," *Energy & Environmental Science* 17, no. 17 (2024): 6368–6376.

86. A. Majid, S. Tasawar, H. Raza, et al., "Uncovering the Potential of Two-Dimensional $SrRuO_3$ as Anode Material in Li, Na, Mg, Ca, K, and Zn Ion Batteries: First-Principles Investigations of Structural, Electronic and Electrochemical Properties," *Journal of Energy Storage* 105 (2025): 114634.

87. A. Majid, U. Najam, S. Ahmad, and M. Alkhedher, "On the Prospects of Using $B_4C_3$ as a Potential Electrode Material for Lithium-Ion Batteries," *Materials Science in Semiconductor Processing* 176 (2024): 108320.

88. A. Majid, B. Khadim, M. Alkhedher, and N. Bulut, "Prospects of Ruthenate-Based Electrodes in Metal-Ion Batteries," *Sustainable Energy & Fuels* 8, no. 18 (2024): 4019–4038.